Preprint Cambridge Centre for Computational Chemical Engineering ISSN 1473 – 4273

Injection of charge from non-thermal plasma into a soot forming laminar coflow diffusion flame

Yong Ren Tan[1,2,3], Yichen Zong[2,3], Maurin Salamanca[4], Jacob W. Martin[5], Jochen A. H. Dreyer[6], Jethro Akroyd[1,2], Wenming Yang[3], Markus Kraft[1,2,7,8]

released: January 7, 2022

[1] Department of Chemical Engineering and Biotechnology
University of Cambridge
Philippa Fawcett Drive
Cambridge, CB3 0AS
United Kingdom

[2] CARES
Cambridge Centre for Advanced Research and Education in Singapore
1 Create Way
CREATE Tower, #05-05
Singapore, 138602

[3] Department of Mechanical Engineering
National University of Singapore
9 Engineering Drive 1
Singapore, 117576

[4] Escuela de Química
Universidad Nacional de Colombia-Sede Medellín
Carrera 65 A No 59A-110
Medellín, Colombia

[5] Department of Physics and Astronomy
Curtin University
Perth WA 6845
Australia

[6] CoaST, Department of Chemical and Biochemical Engineering
Technical University of Denmark
Lyngby, Denmark

[7] School of Chemical and Biomedical Engineering
Nanyang Technological University
62 Nanyang Drive
Singapore, 637459

[8] The Alan Turing Institute
London
United Kingdom

Preprint No. 288

Keywords: Non-thermal plasma, Laminar coflow diffusion flame, Soot, Soot volume fraction, Laser induced incandescence (LII)

Edited by
Computational Modelling Group
Department of Chemical Engineering and Biotechnology
University of Cambridge
Philippa Fawcett Drive
Cambridge, CB3 0AS
United Kingdom

E-Mail: mk306@cam.ac.uk
World Wide Web: https://como.ceb.cam.ac.uk/

Abstract

A novel, modified Yale Steady Flame burner was developed to study the effect of charge injection from a non-thermal plasma into three helium-diluted laminar coflow diffusion ethylene flames. The frequency of the high voltage (HV) signal was varied to control the ion concentration injected into the flames. Optical emission spectroscopy was used to characterise the non-thermal plasma while a bias plate methodology was used to gauge the relative amount of charge generated. For different HV signal frequencies, the laser-induced fluorescence of OH^*, chemiluminescence of CH^*, and laser-induced incandescence of soot in flames were measured. The OH^* and CH^* measurements showed that the flames with the injected charge retained the classic flame shape. This is significant because it can facilitate the study of the effect of charge on the formation of soot in flames. Soot reduction was found to be significant at low HV signal frequencies corresponding to an increase in the amount of the relative charge injection. The soot reduction decreased when the HV signal frequency increased, which corresponded to a drop in the concentration of the ion concentration. Notably, at low HV signal frequency, the magnitude of soot reduction in high concentrated (60%) ethylene flame is three times lower than that of the less concentrated (32%) ethylene flame. This can be attributed to the decrease in the ratio of charge injected to soot precursor concentration when the concentration of the ethylene flame is increased. These results demonstrate that the current system is a promising candidate for studying the effect of the charge from non-thermal plasma on soot formation in laminar coflow diffusion flames.

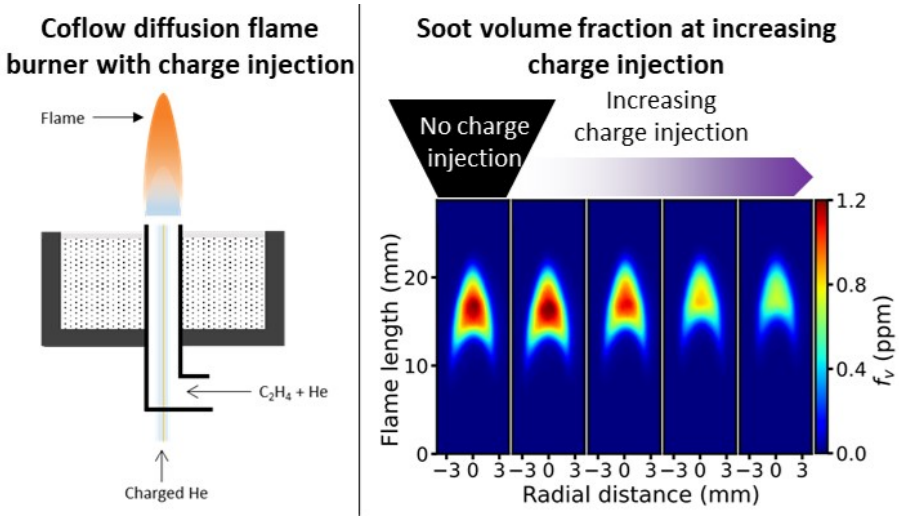

Highlights

- Ethylene coflow diffusion flame with charge injection was reported for the first time
- Flames with injected charge retained the classical flame shape
- The soot volume fraction decreases with increasing charge injection into the flame

Contents

1 Introduction

The formation and consequent emission of soot (*i.e.* particulate matter) from the combustion of fuels into the atmosphere has been demonstrated to cause respiratory disease [19] (including increased COVID-19 mortality [32]) and global warming [29]. This has led to increased efforts to control and eliminate these harmful emissions via a better understanding of the formation of soot during combustion. Intriguingly, the formation of soot was found to be linked to the presence of charged species. This was initially demonstrated by Brande in 1814, by applying an electric field to a flame [3].

Teasing apart the role of ions on soot inception has led to advances in burner design and flame chemistry [16, 37, 41]. Firstly, Weinberg and colleagues realised that an ionic wind dominated Brande's experiments [45]. The ionic wind modified the diffusion flame structure, aerating the flame and thereby reducing soot emissions. They developed a counterflow burner design where the electric field was applied perpendicular to the stagnation surface, allowing the electric field to shift but not significantly alter the soot forming region. This setup has been recently reexamined and shown to demonstrate the role of electric fields on soot inception rates [33, 43]. However, the shift in the stagnation surface does lead to some quenching of reactions that makes decoupling the role of the electric field from an ionic wind less conclusive.

Secondly, easily ionisable species and high voltage (HV) arcs were used to increase ion concentrations in flames, which typically has already a significant amount of charge (*ca.*. 10^4–10^6 ions/m^3 [8]). This normally involves the injection of metal ions [7, 20, 21, 38, 46] or introducing HV arcs [10] into the flame. However, these approaches were found to alter the chemistry and structure of the flame. For example, metal ions were found to induce stabilisation of small soot nuclei which in turn increase the oxidation rate of smaller particulates with the increase in the available particulate surface area [23]. The use of HV arc-discharges was also explored by Weinberg and others [24, 48, 51]. Nevertheless, several changes can occur simultaneously with plasma discharges. This includes the chemionisation by charged particles, gas heating, ionic wind, generation of turbulence by pulsed discharges and radical generation ahead of the flame front [24, 48].

Most recently, non-thermal plasmas that allow for the decoupling of the electron and ion temperatures have been developed [36]. These non-thermal plasmas generate high concentration of low-temperature ions with low-power consumption [36]. Cha et al. first demonstrated the impact of non-thermal plasma on soot formation using an electrode placed in the centre of a coflow diffusion flame [10]. Significant decreases in soot formation were demonstrated. However, the flame structure was significantly perturbed by the the plasma discharges. With increased plasma generation, the flame changed shape from near conical to crown. The electrode also inhibited optical interrogation and built up soot deposits over time.

The **purpose of this paper** is to report a novel, modified Yale Steady Flame burner that is integrated with a charge injection system from a non-thermal plasma for the investigation of the impact of charge on soot formation, with minimal impact on the flame structure. Notably, the charge injection system is based on the recent advances in non-thermal plasma jets [31], which allow the separation of the charge generation from the

flame front. In particular, the effect of varying concentrations of excited helium ions for different helium dilution ratios of the ethylene coflow diffusion flames on soot volume fraction is investigated.

2 Experimental

2.1 Laminar coflow diffusion flame

The base flame is an atmospheric-pressure helium-diluted laminar coflow diffusion ethylene flame, generated using a modified Yale Steady Flame burner [47], as shown in Figure 1.

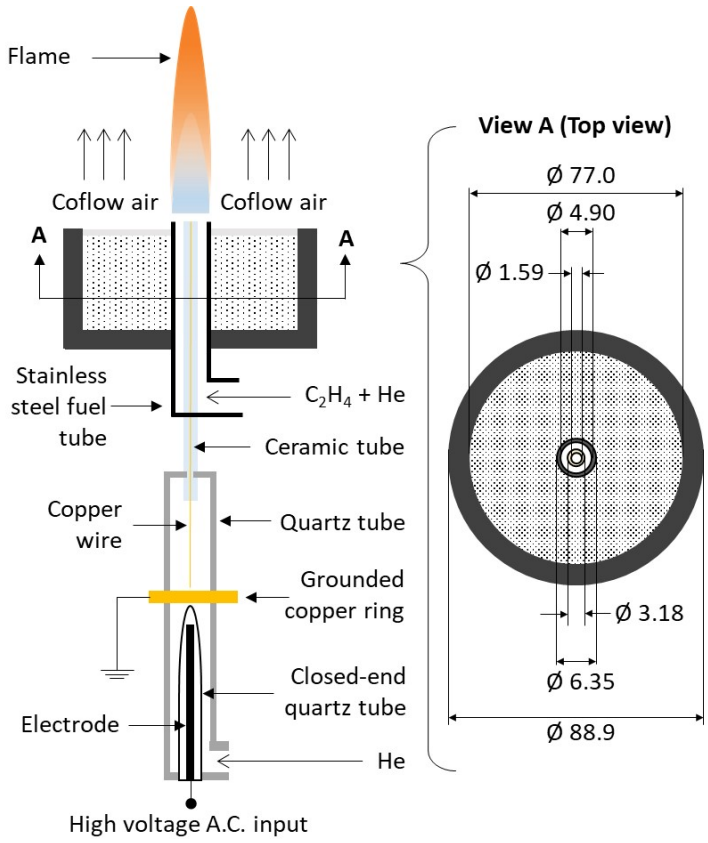

Figure 1: *Schematic of the coflow diffusion flame burner setup. Charge from non-thermal plasma is injected into the flame via a ceramic tube that is concentric to the fuel tube. The diameter measurements (Ø) of the burner, fuel tube and charge injection tube are given in millimetres under the top view version of the burner.*

The stainless steel fuel tube has an inner diameter of 4.90 mm and an outer diameter of 6.35 mm. A 3.18 mm OMEGATITE^{TM} 450 ceramic tube (Omega Engineering Inc.) with an inner diameter of 1.59 mm is placed concentrically within the fuel tube to deliver

charge into the flame. The gas flow rates are reported in Table 1. The overall cold gas velocity for the fuel and air was maintained at 35 cm/s. The ethylene and helium were supplied from 99.99% purity cylinders. The coflow air (95 slm) was supplied through a concentric coflow tube with an inner diameter of 74.0 mm, fitted with a stainless steel honeycomb mesh (0.43 mm wall thickness, 18×18 mesh). The resulting flames were lifted above the fuel tube by about 2 mm.

Table 1: *Flow rates (sccm) of helium-diluted ethylene flames.*

Concentration % of ethylene	32%	40%	60%
Ethylene flow rate	78.7	98.4	147.6
Fuel tube helium flow rate	167.3	147.6	98.4
Charged helium flow rate	40.0	40.0	40.0

2.2 Non-thermal plasma generation

The design of the non-thermal plasma generator is based on the plasma jet generator reported by Kostov et al. [31]. A high voltage (HV) signal is generated using a Minipuls4 (GBS Elektronik GmbH) pulse generator controlled by a PicoScope® 2205A oscilloscope (Pico® Technology Ltd.). The HV signal is connected to a copper electrode that is enclosed in the inner closed-ended part of a concentric quartz tube, as shown in Figure 1. The inner part of the tube acts as a dielectric barrier between the electrode and helium flowing through the outer part of the tube. The helium is ionised by the HV signal (at frequencies of 22-25kHz) and flows from the quartz tube to the burner. The ion concentration was controlled by altering the HV frequency at 22-25 kHz. It is measured using an established methodology [18] with a helium flow rate of 400 sccm. A detailed description of the HV signal generation and operation of the non-thermal plasma generator is given in Section S1 of the Supplementary material. Notably, the naming convention for the case without any charge injection (*i.e.* no HV and at frequency of 0 kHz) is 'No HV'. The ion concentration measurements are reported in Section S2. An electrical characterisation of the plasma generated is presented in the Section S3. The non-thermal nature of the plasma was demonstrated by measuring minimal heating of the ceramic tube within which the plasma was generated.

2.3 Optical emission spectroscopy and chemiluminescence

The emission spectra of the plasma generated were recorded using an Andor Kymera 328i spectrometer (Oxford Instruments plc.) in the range 440–960 nm at 40 sccm of helium without ignited flame. The measurements were performed perpendicular to the axis of the charge delivery ceramic tube.

The excited-state CH radicals ($A^2\Delta$, denoted as CH^*) of the flames were measured using an intensified charge-coupled device (ICCD) camera from LaVision, coupled with narrow-bandpass filters (420, 430 and 440 nm with FWHM = 10 nm). The data were processed to give two-dimensional radial distributions using the two-filter subtraction proce-

dure [28, 35] followed by an inverse Abel transform [12, 15]. The observed standard error was 10–15%.

2.4 Laser measurements

A Nd:YAG laser (Quantel Q-smart, 5 ns pulses at 10 Hz) at 532 nm was used to perform laser-induced incandescence (LII) measurements of the soot volume fraction (f_v) in the flames, see Figure S4.4 in the Supplementary material. A laser fluence of 0.18 J/cm^2 was used to ensure that the signal was in the saturation regime [11]. A bandpass filter with center wavelength of 405 nm and bandwidth of 70 nm was used before the ICCD camera. The camera gate was set to 50 ns to avoid overestimation of the signal from large particles, and the camera delay set to 80 ns to maximise the signal-noise ratio. The uncertainty of the f_v measurements were found to be $\pm$10%.

Laser-induced fluorescence (LIF) measurements were performed using the same system with a dye laser (Quantel Q-scan) at 283.25 nm, to obtain the distribution of excited state OH ($A^2\sum$, denoted as OH*) in the flames [42]. A bandpass filter (LaVision, VZ-image 308 nm; FWHM = 10 nm; and transmissivity >60%) was used before the ICCD camera. The camera gate was set to 100 ns and delay to 30 ns. The OH-PLIF measurements were found to have standard error of 10-–15%. A detailed description of the LII and LIF laser system can be found in the Section S4.

3 Results and discussion

3.1 Characterisation of non-thermal plasma

Figure 2 shows the optical emission spectra of the electronically excited gas-phase helium (He I) without charge injection (*i.e.* no HV) and with charge injection with HV frequencies of 22, 23, 24 and 25 kHz. There is a clear and high intensity peak at 706.1 nm (Peak 'e' in Figure 2), which is characteristic of the He I. Notably, the intensity of the peak decreases with the increase in the HV frequency from 22 kHz to 25 kHz [31, 53]. The amount of He I generated decreases with the increase in the HV frequency in this range.

The amplitude of the voltage and current signal of the plasma decreases with the increase in HV frequency (see Figure S3.3). The discharge power is correlated with the amplitude of the voltage and current waveforms [31, 53], and it is therefore expected that the increase in the HV frequency would result in fewer helium atoms being electronically excited. This is consistent with the findings from Figure 2. Additionally, the temperature of the non-thermal plasma was measured to be *ca.*. 303 K, again consistent with the literature [30, 31]. Hence, it is expected that the injection of the charge from the non-thermal plasma has an insignificant thermal effect on the flame.

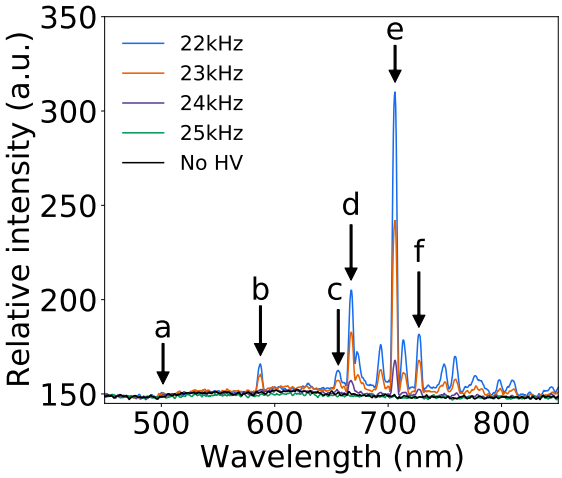

Figure 2: *Emission spectra of plasma at no HV and different HV frequencies. Peaks a–f: He I. The colour version of the figure is available in the online version of this paper.*

3.2 Effect of charge from non-thermal plasma on flame structure

The effect of injecting charge from non-thermal plasma on the flame structure was analysed using the OH^* and CH^* distributions, both of which provide a reasonable visual representation of the structure and position of a flame [9, 35, 49]. One of the challenges of studying the effect of charge from non-thermal plasma on soot formation in laminar flames is that the non-thermal plasma can induce significant changes in the shape of the flame [10]. In the current study, it was observed that all the flames maintained the same well-defined laminar flame structure, *i.e.* a blue flame sheet and a dim blue hollow interior in the lower part of the flame, and luminous closed-tip yellow tongue (attributed to soot) at the upper part of the flame [9] (see Figure S5.6 of the Supplementary material), independent of the injection of charge.

Figure 3 shows the OH^*-PLIF signals. The OH^* region can reasonably represent the soot oxidation zone [1, 10, 17, 26] and acts as a marker for the upper part of the flame [1]. The formation of OH^* in hydrocarbon flames typically occurs via [6]

$$CH + O_2 \longrightarrow CO + OH^*. \tag{1}$$

It was observed that the OH^* was distributed in the outer region of all the flames, consistent with the shape of typical laminar coflow diffusion flames.

Notwithstanding that the general shape of the laminar flame is preserved, the details of the flame geometry differ with the HV frequency. Notably, the flames with charge injection at a lower frequencies (*i.e.* 22 kHz and 23 kHz) bulge in the mid-part of the flame and have an elongated arch, causing an increase in the flame diameter. The intensity of the OH^*-PLIF signal increases, yet occupies a narrower region of the flame. Generally, the OH^* distribution is considered to be a good indicator of the region of high-temperature oxidation [26]. This may indicate that the flames with high charge concentration show a slight enhancement in oxidation.

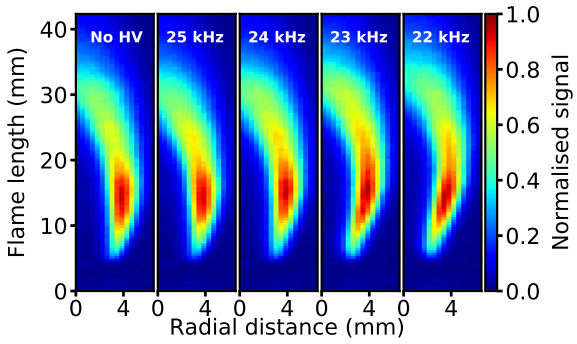

(a) 32% ethylene flames at different HV frequencies.

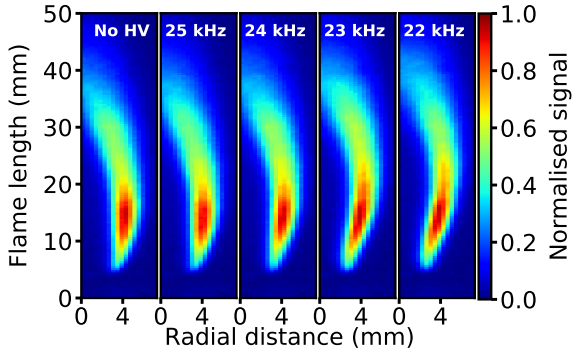

(b) 40% ethylene flames at different HV frequencies.

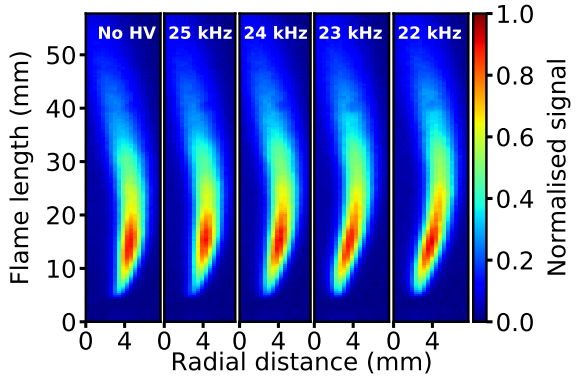

(c) 60% ethylene flames at different HV frequencies.

Figure 3: *OH*-PLIF profiles of the (a) 32%, (b) 40% and (c) 60% ethylene flames without charge injection (No HV) and with charge injection at different HV frequencies. The HV frequency is indicated at the top of each image. The intensities of the OH* have been normalised by their respective maximum values.*

Figure 4 shows the CH* distribution in the lower part of the flames (*i.e.* the flame anchoring region), close to the fuel tube. CH* is a significant indicator of the lower part of the flame front (typically indicated by a blue flame sheet) and a marker of the com-

pletion of fuel degradation [34, 50]. Only the lower part of the flames is shown because only this region has a strong CH* signal. The proximity to the point of charge injection means that this region is of particular interest in the current study. In the current flames, the CH* region extends close to the fuel tube and forms a thin flame front downstream of the flame. This indicates that the flames remain intact despite the presence of the charge, complementing to the findings of Figure 3 which focused on the downstream region.

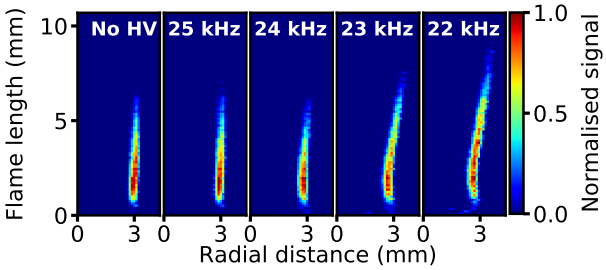

(a) 32% ethylene flames at different HV frequencies.

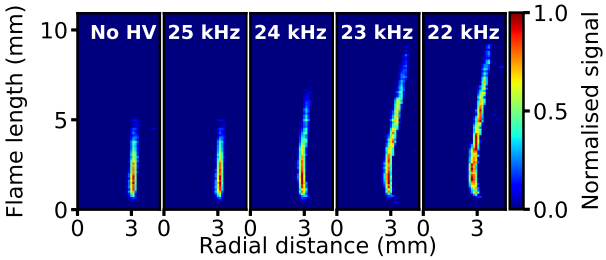

(b) 40% ethylene flames at different HV frequencies.

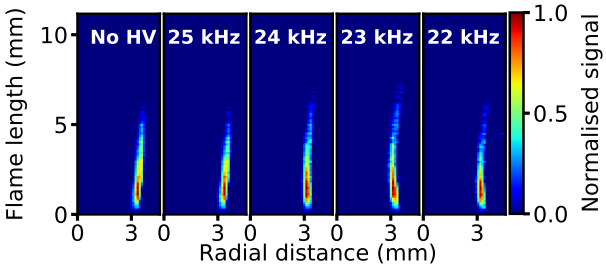

(c) 60% ethylene flames at different HV frequencies.

Figure 4: *The CH* chemiluminescence profiles of the (a) 32%, (b) 40% and (c) 60% ethylene flames without charge injection (No HV) and with charge injection at different HV frequencies. The frequency is indicated at the top of each image. The intensities of the CH* have been normalised by their respective maximum values.*

A detailed examination of the CH* distribution in Figure 4(a) shows that the charge has some effect on the upstream region of the flames. In the flames without charge injection (no HV), the maximum CH* signal intensity is observed in a relatively compact area.

The 32% ethylene flame has a wider signal region than the 40% and 60% flames, consistent with the smaller 'blue' region observed in more sooty (60% ethylene) flames. In the flames with charge injection at 22 and 23 kHz HV frequencies, the signal curves towards the centre-line and shows an increased area with normalised CH^* intensity, accompanied by a decrease in the value of the maximum intensity (see Figure S6.7 of the Supplementary material). In quantitative terms, the maximum intensity decreased by 19% from the case without charge injection (No HV) to the case with the highest charge injection (HV frequency of 22 kHz) for the 32% ethylene flame. The curvature of the signal towards the centre-line and the area of high normalised CH^* intensity decreased as the HV frequency was further increased to 24 and 25 kHz, accompanied by an increase in the value of the maximum intensity. By 25 kHz, the CH^* distribution and maximum signal intensity had reverted to be similar to that observed in the (No HV) flame without charge injection. Similar behaviour was observed for the 40% and 60% ethylene flames.

3.3 Effect of charge on soot formation

Figure 5 shows the spatial distribution of the soot volume fraction, f_v, obtained from LII measurements for the 32%, 40% and 60% ethylene flames. The 32% ethylene flame has a maximum centre-line soot volume fraction of 1.2 ppm at 0 kHz, which is within the expected range (*ca.*. 1.4 ppm) of soot volume fractions measured for helium-diluted ethylene flames using colour-ratio pyrometry [25]. The maximum soot volume fraction at the centre-line was observed to drop with the decrease in the HV frequency from 25 to 22 kHz. At 22 kHz, the maximum soot volume fraction at the centre-line has already decreased to 0.7 ppm. This is attributed to the increased amount of ionised helium injected into the flame as the HV frequency is decreased from 25 to 22 kHz. Notably, both the 40% and 60% diluted ethylene flames showed similar but reduced trends with the change in HV frequency.

Figure 6 (left axis) shows the normalised maximum soot volume fraction in the flames versus HV frequency. The normalisation is based on the corresponding (0 kHz) flame without charge injection for each ethylene flow rate. Meanwhile, Figure 6 (right axis) shows the relative ion concentration measured versus HV frequency. The error bars are representative of the standard error from six repetitions for each of the measurements.

In general, the reduction in the soot volume fraction at a given HV frequency decreases as the quantity of ethylene increases. For example, at 22 kHz, the reduction in soot volume fraction in the 32% ethylene flame is more than three times that for the 60% ethylene flame. The magnitude of the reduction in soot volume fraction decreases as the HV frequency is increased. By 25 kHz, the change in the soot volume fraction is negligible. This correlates with the reduction in the relative ion concentration of the charge injection as the frequency is increased from 22 to 25 kHz, as shown on the right axis of Figure 6.

Several insights into the effect of charge on soot formation can be inferred from Figure 6. At an HV frequency of 25 kHz, the ion concentration is too low to have a discernible effect on soot reduction in the ethylene flames studied. When the HV frequency is progressively reduced to 22 kHz, an increasing concentration of ions is injected into the flames. This is more pronounced in the 32% ethylene flames compared to the 40% and 60% ethylene

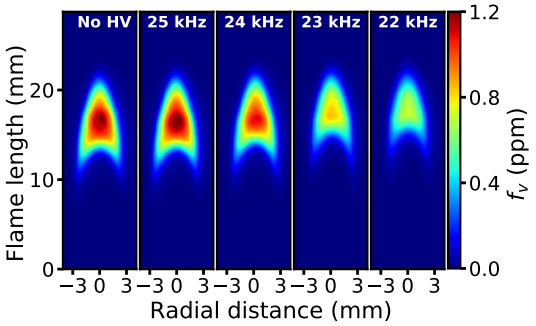

(a) 32% ethylene flames at different HV frequencies.

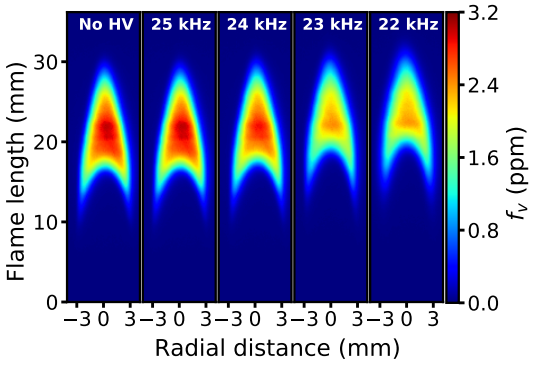

(b) 40% ethylene flames at different HV frequencies.

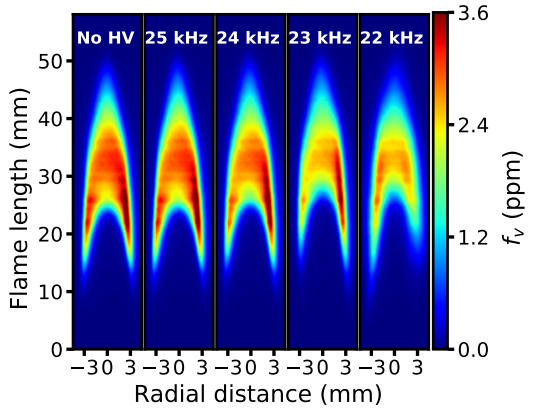

(c) 60% ethylene flames at different HV frequencies.

Figure 5: *Soot volume fraction, f_v, in the (a) 32%, (b) 40% and (c) 60% ethylene flames without charge injection (No HV) and with charge injection at different HV frequencies. The HV frequency is indicated at the top of each image.*

flames. This is attributed to an increase in the concentration of soot precursors when the proportion of ethylene is increased. Since the charge injection (ion concentration) was kept constant (at a given frequency) for all flames, the relative concentration of ions to

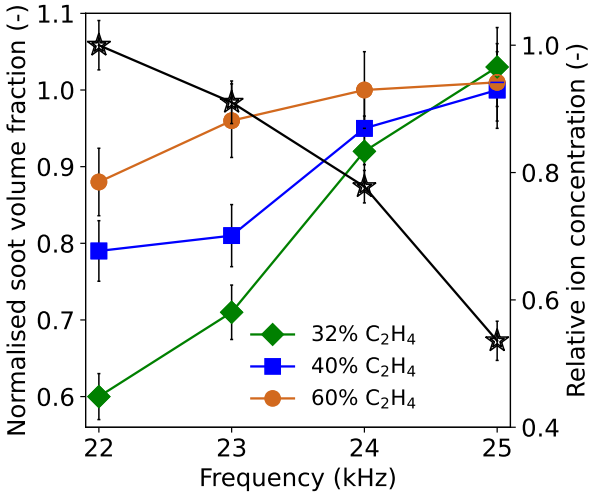

Figure 6: *Left axis: Normalised maximum soot volume fraction (f_v) versus HV frequency for the He-diluted 32%, 40% and 60% ethylene flames. The normalisation is based on the maximum soot volume fraction observed in each flames without charge injection. The error bars show the standard error for each of the measurements. The lines are drawn to guide the eye. Right axis: Relative ion concentration of the charge injection.*

soot precursors decreases as the ethylene is increased from 32% to 40% and 60%.

The charge generated from the non-thermal plasma in the current experiments could form He^+ and He^* (electronically excited He). These species can consequently undergo rapid conversion into relatively stable helium dimer ions (He_2^+) [5]

$$2\,He + He^+ \longrightarrow {He_2}^+ + He, \tag{2}$$

$$He^* + He \longrightarrow {He_2}^+ + e^-. \tag{3}$$

The helium dimer ion (He_2^+), being positively charged, may impact the formation of soot, possibly through four routes:

- Alter the fuel breakdown (pyrolysis) [13].
- Modify the flame chemistry through ionic reactions [24]. The increase of the CH^* may indicate some influence on C1-C3 ionic reactions or fuel breakdown.
- Disrupt the primary particle aggregation (second mode) [14].
- Modify the particle inception through ion-induced nucleation (first mode) [2, 39, 40].

Understanding the interplay of these contributions on the formation of soot is an ongoing effort. Nevertheless, the proposed burner design met its objective of providing a laminar coflow diffusion flame with charge injection and minimal modifications to the flame structure, thus providing a new target flame for studying the impact of charge on soot formation and destruction.

4 Conclusions

A modified Yale Steady Flame burner has been developed to study the effect of injecting charge from non-thermal plasma on soot formation in laminar coflow diffusion flames. Charged helium was generated using a plasma excitation system operating with high voltage (HV) frequencies from 22 to 25 kHz. The concentration of charged helium was observed to decrease as the frequency increased from 22 to 25 kHz.

The charged helium was injected through a coaxial concentric fuel tube arrangement into helium-diluted 32%, 40% and 60% ethylene flames. The soot volume fraction and OH^* distribution in the flames was measured using laser-induced incandescence and laser-induced fluorescence, respectively. The chemiluminescence of the CH^* distribution was measured using an intensified charge-coupled device camera. The data were analysed to investigate the impact of charge on the soot volume fraction in the flames.

The OH^* and CH^* profiles were analysed versus the HV frequency used to generate the charge. Both of them showed that the flames injected with the charged helium retained their classic laminar flame shape, indicating that the burner achieves its objective of minimising disruption to the flame, so facilitating the study of soot formation.

The soot volume fraction was analysed versus the HV frequency. The soot reduction was most pronounced when the 32% ethylene flame was injected with charge generated at 22 kHz. The level of reduction decreased as both the HV frequency and proportion of ethylene were increased. The increase in HV frequency reduced the ion concentration injected into the flames, while the increase in the proportion of ethylene increases the soot precursor concentration, such that decrease in the soot reduction is consistent with a decrease in the ratio of the ion to soot precursor concentration.

The preservation of the overall laminar flame shape and the observed reduction in the soot volume fraction suggest that the current system is a good candidate to study the impact of charge on the formation of soot in a laminar coflow diffusion flames and therefore serving as a potential target flame for the modelling community. Further experimental and modelling investigations are needed to understand the link between charged species and the formation of soot.

Acknowledgements

This research was supported by the National Research Foundation, Prime Minister's Office, Singapore under its Campus for Research Excellence and Technological Enterprise (CREATE) programme. Y. R. Tan acknowledges financial support from Fitzwilliam College Cambridge, Trinity College Cambridge and the Cambridge Trust. M. Kraft gratefully acknowledges the support of the Alexander von Humboldt Foundation. M. Salamanca is grateful with Universidad Nacional de Colombia-Sede Medellín for its support. The authors thank Dr Taniela Lolohea from the School of Chemical Sciences, Auckland University of Technology for advice about non-thermal plasma; and Prof. Allan N. Hayhurst from the Department of Chemical Engineering and Biotechnology, University of Cambridge for advice about ion measurements in flames.

Supplementary material

S1 Principle of non-thermal plasma operation and setup

Plasma, a mixture of positive ions and free electrons, is the fourth state of matter. It occurs naturally, *i.e.* during lightning or in stars, but can also be generated artificially [44]. All methods for plasma generation require some kind of energy input, either in the form of elevated temperatures or an electric field. Additional distinctions can be made based on the temperature and pressure of the obtained plasma [4, 36, 52].

The aim of this study is to develop a burner system that can investigate the influence of charge on soot formation in flames. Ideally, the system should therefore not alter anything (especially the flame temperature and the flame geometry) except for the amount of electric charge in the flame. Any technique that generates a hot plasma, distorts the flame via electric wind effects, or operates at low pressures is therefore not suitable.

Techniques that meet the above requirements are referred to as cold atmospheric plasma, which is also known as non-thermal plasma [36]. Within this group of plasmas, distinctions are made depending on the geometry and arrangement of the electrodes, the employed gases, and the operating voltages and supply frequencies. Both for safety reasons and to avoid arcing, dielectric barrier discharge (DBD) plasma generators are preferred because the high voltage (HV) electrodes are covered with a dielectric material [4]. DBD plasma generators have also been described in the literature, in combination with floating electrodes to aid plasma transport through flexible tubes [30, 31]. This methodology facilitates the generation of plasma far away from where it is ejected, making it ideal for charge injection from plasma into flames. Any electric wind effects due to electric fields around the electrodes can be avoided and the charge can be injected into the centre of axisymmetric flames without breaking their symmetry.

In light of these considerations, a plasma generator was constructed based on reports of cold atmospheric plasma jets exiting from long flexible tubing [30, 31]. Figure S1.1 shows a schematic of the setup. The same HV power generator and similar materials, geometries, gases, supply voltages and frequencies were employed. The HV generator consists of several components that are based on the setup in the literature [30, 31]. A power supply (TDK-Lambda LS200 Series) was used to convert the 230 V A.C. input to a 24 V D.C. output which goes to the Minipuls4 (GBS Elektronik GmbH) pulse generator set. The Minipuls4 pulse generator set, which consists of a full bridge converter and a transformer cascade then converts a 24 V D.C. input to an HV A.C. output. The frequency signal of the HV A.C. output is provided via a PicoScope® 2205A oscilloscope (Pico® Technology Ltd.) where the signal is amplified using a NE5532 pre-amplifier (ON Semiconductor®) before being provided as an input to the Minipuls4. The square waveform generated with the Picoscope® was amplified to amplitudes of +5 V and -5 V to oscillate the polarity of the Minipuls4 HV output. The frequency of the plasma generation and the shape of the signal waveform is controlled using the PicoScope® 6 PC Oscilloscope (Version 6.14.36.5676) software. The temperature of the non-thermal plasma was measured to be *ca.*. 303 K.

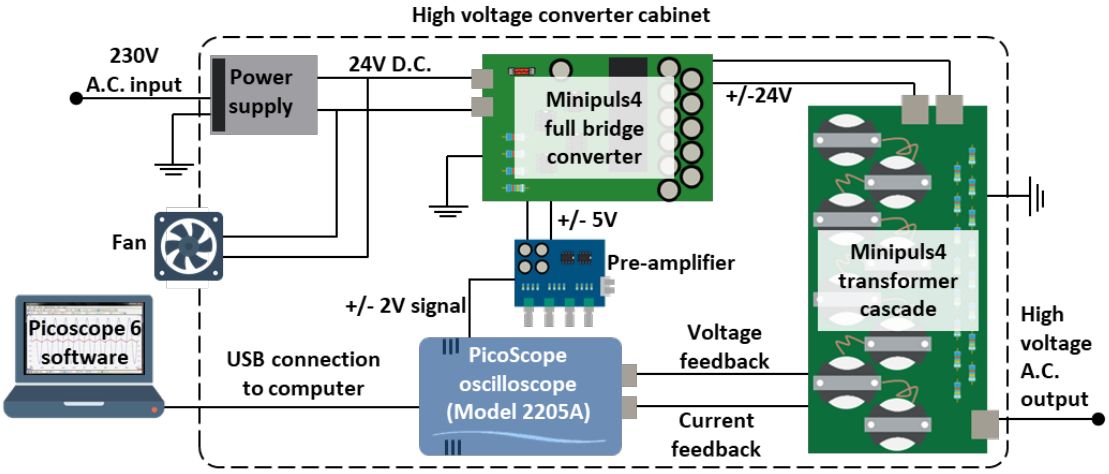

Figure S1.1: *Schematic of the electric circuit setup for the high voltage generator. A.C. = Alternating current; D.C. = Direct current; USB = Universal serial bus.*

S2 Ion concentration measurement

The ion concentration of the charge injected from the non-thermal plasma was measured using an established methodology [18] that provides a convenient method to measure ions in a burner. A diagram of the measurement setup is as shown in Figure S2.2. It infers the concentration of ions by measuring the current produced by the flow of ions. A power supply unit (CHUX®, 100 V, 3 A) is used to apply a potential difference between a measurement plate and the burner. A digital multimeter (Keithley, Model 2000) is used to measure the current between the electrodes. Due to the low number of ions produced, it was necessary to use higher flow rates of helium (400 sccm) when measuring the ion concentration compared to the experiments reported in the main text. On the assumption that the flow rate of helium is related to the number of ionised species, the concentration at lower helium flow rate (40 sccm) is expected to be lower than the case at 400 sccm helium flow rate [22].

S3 Electrical characterisation of non-thermal plasma

The voltage-current characteristic as a function of time is reported by PicoScope® 2205A oscilloscope (Pico® Technology Ltd.) via the PicoScope® 6 PC Oscilloscope (Version 6.14) software. Figure S3.3 shows the waveforms of the applied voltage and the corresponding discharge current as a function of time at different HV signal frequencies. The amplitude of the voltage and current signal decreases as the frequency increases. The discharge power is correlated to the amplitude of the voltage and current waveforms [31, 53]. There is a decrease in the amplitude (and discharge power) per cycle as the frequency increases because the plasma generator has a fixed amount of discharge power in a fixed time period.

The waveform of the discharge current lags the applied voltage by 90°, *i.e.* the current discharge starts to occur only at the peak of the applied voltage. The mechanism re-

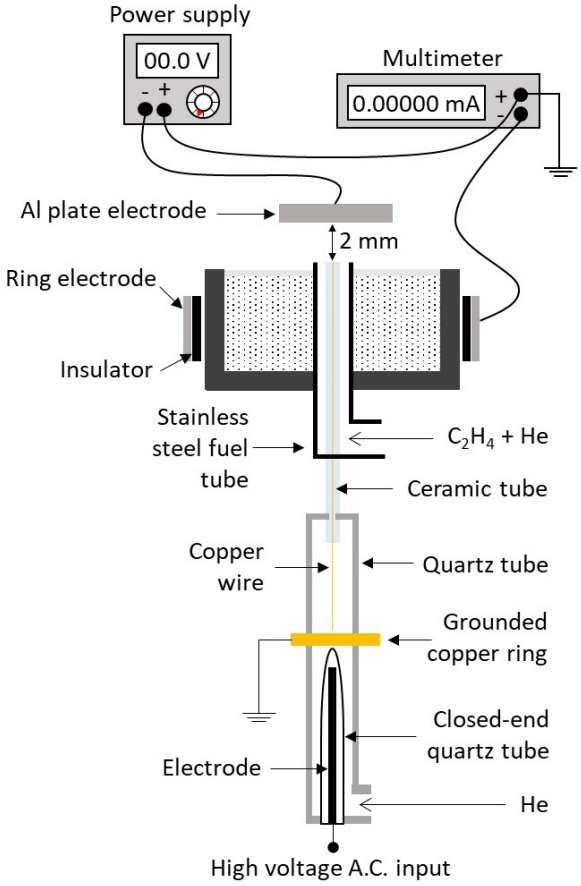

Figure S2.2: *Schematic of the experimental setup of the measurement of ions from the plasma jet. A.C. = Alternating current.*

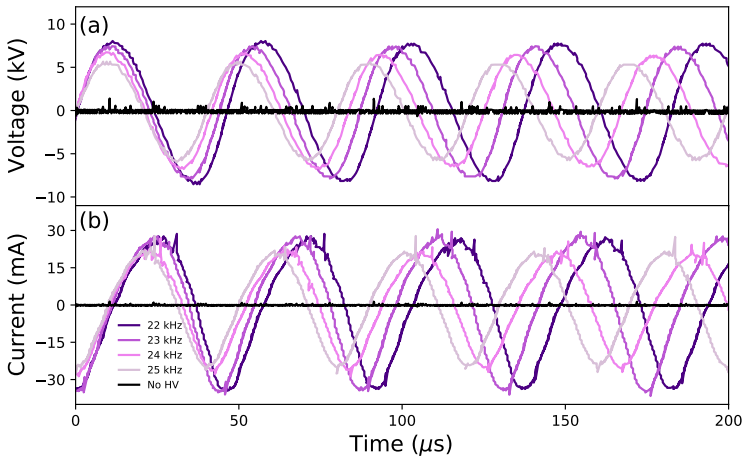

Figure S3.3: *The waveforms of the (a) applied voltage and (b) discharge current recorded in a time interval.*

sponsible for this is described in detail in the literature [31]. A brief explanation is that,

when the applied voltage is positive and reaches a threshold for gas ionisation, the electrode will become an anode. This will result in a cathode-directed streamer discharge maintained by photoionisation [27, 31]. Electrons will propagate from the cathode to the anode, resulting in a positive current. When the polarity of the voltage is negative, the electrode becomes a cathode, resulting in an anode-directed streamer maintained by secondary electron avalanches [27, 31]. The electron movement is reversed, resulting in a negative current. Additionally, the peaks of the waveform form for the discharge current show some irregularities. This is typical of plasma discharge [31, 54].

S4 Laser system

S4.1 Laser-induced incandescence measurements

Figure S4.4 shows a schematic of the laser-induced incandescence (LII) measurements of the coflow diffusion flames. The Nd:YAG laser (Quantel Q-smart, Wavelength: 532 nm, Pulse width: 5 ns, Repetition rate: 10 Hz) at 532 nm is used to perform the measurements. The laser beam is initially turned 90° by a beam steering prism. Then, it is transformed into a vertical planar laser sheet with a narrow cross-sectional area of 40 mm by 0.5 mm and focused across the centre-line of the burner using LaVision sheet optics (two telescope lenses and one divergent lens). The laser fluence was monitored and recorded with an energy meter (Coherent® FieldMaxII-TOP™) before the setup of the Lavision sheet optics. The averaged laser fluence was found to be 0.18 J/cm^3 for the 532 nm laser. The laser fluence was used to ensure the signal is in the saturation regime [11].

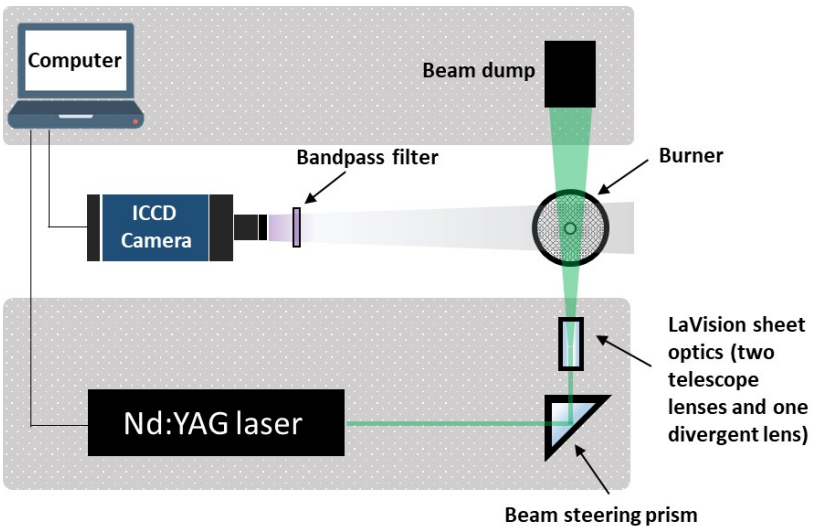

Figure S4.4: *Schematic of the laser system setup for laser-induced incandescence (LII) measurements.*

The LII signal is collected normal to the laser beam using the camera setup shown in

Figure S4.4. A broad bandpass filter (LaVision GmbH, Centre wavelength: 405 nm, Bandwidth: 70 nm) is used before the intensified charge-coupled device (CCD) camera. The intensified CCD camera includes intensified relay optics (LaVision GmbH) and a CCD camera (LaVision GmbH, Imager SX 4M, 12-bit, 2360×1776 pixels). The resultant pixel resolution is 8 px/mm. The camera is accurately controlled and synchronised with the laser using DaVis software (LaVision GmbH, Version 8.1) to record the images. A short camera gate of 50 ns is used in the measurements to avoid the overestimation of signals from large particles. The camera delay is set to 80 ns for the best signal–noise ratio. The flame images were extracted and stored by a digital frame grabber, and 150 images used for each measurement.

S4.2 Laser-induced fluorescence measurements

Figure S4.5 shows the schematic of the laser-induced fluorescence (LIF) measurements of the coflow diffusion flames. A dye laser (Quantel Q-Scan, Sirah PrecisionScan, Rhodamine 590 dye) was used for LIF excitation of OH. The dye laser was pumped by a pulsed Nd:YAG laser (Quantel Q-smart, wavelength: 532 nm, pulse width: 5 ns, repetition rate: 10 Hz). The second harmonic from the 532 nm Nd:YAG laser was passed through a frequency doubler and a dye cell inside the dye laser, providing 10.8 mJ/pulse in the ultraviolet (UV) regime. The laser wavelength of 283.25 nm was used for the OH excitation, which corresponds to the Q1(6) transition of the $A^2\Sigma^2$-$X^2\Pi(1, 0)$ band of OH radical ($A^2\sum$, denoted as OH^*) [42]. The method to focus the laser beam to the centre-line of the burner and the method to measure the laser fluence have been detailed in Section S4.1.

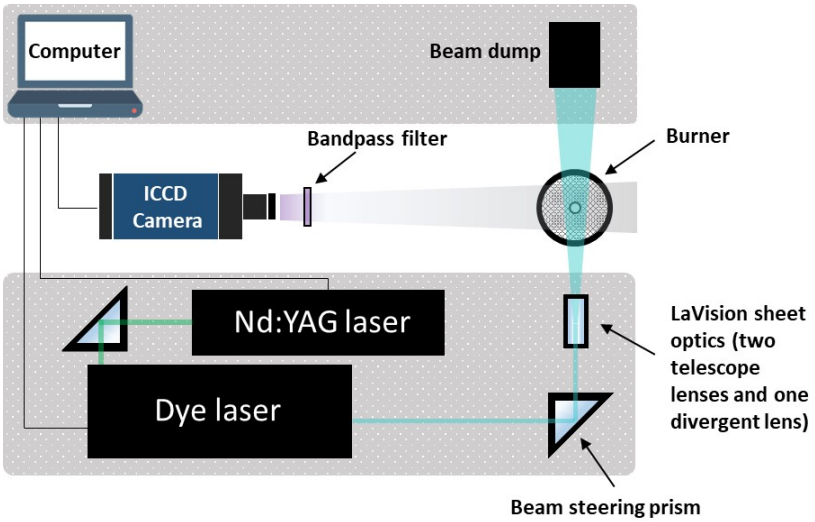

Figure S4.5: *Schematic of the laser system setup for laser-induced fluorescence (LIF) measurements.*

The OH^*-PLIF signal was collected normal to the laser beam using the camera setup

shown in Figure S4.5. A LaVision UV lens (f=85mm, F=2.8), a bandpass filter (LaVision, VZ-image Filter LIF for OH, 308 nm; FWHM = 10 nm; and transmissivity >60%) were used to obtain clear OH*-PLIF signals without scattering of laser light from the dye laser. The OH*-PLIF signals were collected using the intensified CCD camera detailed in Section S4.1, with the camera gate set to 100 ns and delay to 30 ns for the best signal intensity.

S5 Colour images of flames and visible flame lengths

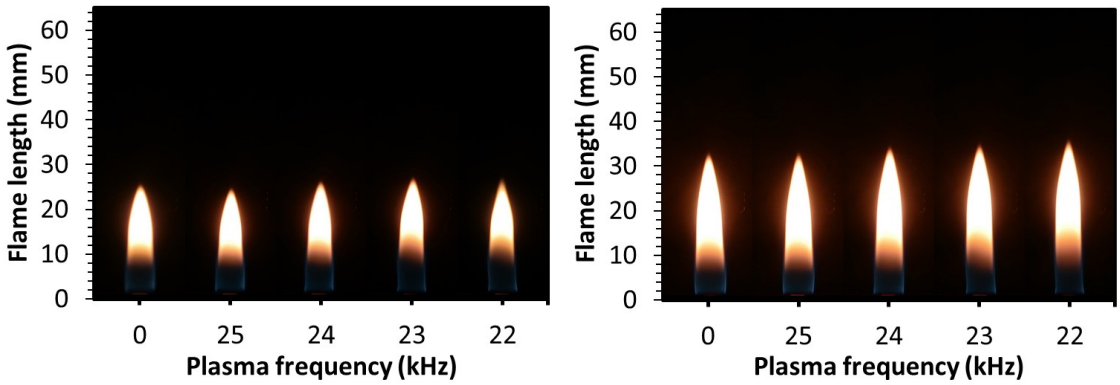

(a) 32% ethylene flames.

(b) 40% ethylene flames.

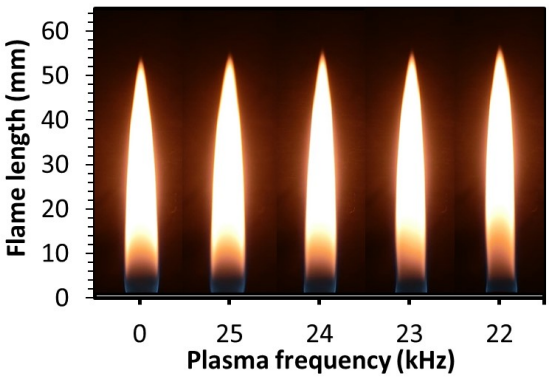

(c) 60% ethylene flames.

Figure S5.6: *Colour images and lengths of the charge-injected ethylene flames at different high voltage frequencies. The images were taken using a Casio EX-ZR5000 colour camera with an exposure time of 0.02 s and ISO speed of ISO-80.*

S6 Methylidyne chemiluminescence distribution

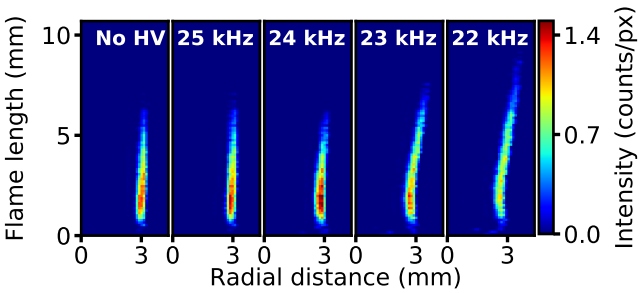

(a) 32% ethylene flames.

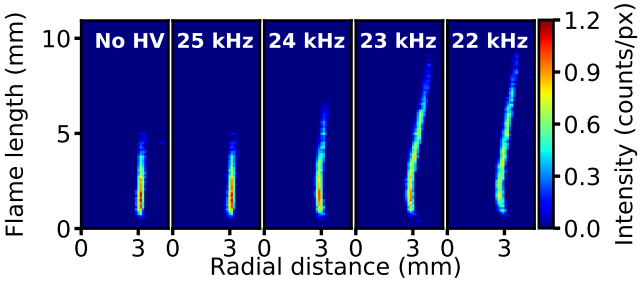

(b) 40% ethylene flames.

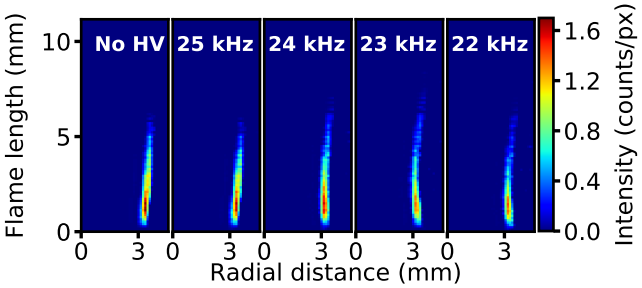

(c) 60% ethylene flames.

Figure S6.7: *The methylidyne (CH^*) chemiluminescence profiles of the (a) 32%, (b) 40% and (c) 60% ethylene flames without charge injection (no HV) and at different high voltage frequencies. The frequency is indicated at the top of each image. The intensities reported for the CH^* are after processing using inverse Abel transformation [12, 15].*

References

[1] M. Ahn, D. Lim, T. Kim, and Y. Yoon. Pinch-off process of Burke–Schumann flame under acoustic excitation. *Combust. Flame*, 231:111478, 2021. doi:10.1016/j.combustflame.2021.111478.

[2] K. Bowal, J. W. Martin, A. J. Misquitta, and M. Kraft. Ion-induced soot nucleation using a new potential for curved aromatics. *Combust. Sci. Technol.*, 191(5-6):747–765, 2019. doi:10.1080/00102202.2019.1565496.

[3] W. T. Brande. XXII. On some new electro-chemical phenomena. *Philos. Mag. Lett.*, 44(196):124–130, 1814. doi:10.1080/14786441408637425.

[4] R. Brandenburg. Dielectric barrier discharges: progress on plasma sources and on the understanding of regimes and single filaments. *Plasma Sources Sci. Technol.*, 26 (5):053001, 2017. doi:10.1088/1361-6595/aa6426.

[5] F. Brandi, L. Labate, D. Rapagnani, R. Buompanea, A. di Leva, L. Gialanella, and L. A. Gizzi. Optical and spectroscopic study of a supersonic flowing helium plasma: energy transport in the afterglow. *Sci. Rep.*, 10:5087, 2020. doi:10.1038/s41598-020-61988-y.

[6] H. P. Broida, A. G. Gaydon, and A. C. Egerton. The mechanism of formation of OH, CH and HCO in flame spectra, using deuterium as tracer. *Proc. R. Soc. Lond. A*, 218(1132):60–69, 1953. doi:10.1098/rspa.1953.0087.

[7] N. A. Burdett and A. N. Hayhurst. Kinetic and thermodynamic measurements of the reactions of the positive ions, Mn^+ and $MnOH^+$, formed by adding manganese to fuel-rich flames of either $H_2 + O_2$ or $C_2H_2 + O_2$. *Combust. Flame*, 189:315–324, 2018. doi:10.1016/j.combustflame.2017.10.022.

[8] H. F. Calcote, D. B. Olson, and D. G. Keil. Are ions important in soot formation? *Energy Fuels*, 2(4):494–504, 1988. doi:10.1021/ef00010a016.

[9] S. Cao, B. Ma, D. Giassi, B. A. V. Bennett, M. B. Long, and M. D. Smooke. Effects of pressure and fuel dilution on coflow laminar methane–air diffusion flames: A computational and experimental study. *Combust. Theory Model.*, 22(2):316–337, 2018. doi:10.1080/13647830.2017.1403051.

[10] M. S. Cha, S. M. Lee, K. T. Kim, and S. H. Chung. Soot suppression by nonthermal plasma in coflow jet diffusion flames using a dielectric barrier discharge. *Combust. Flame*, 141(4):438–447, 2005. doi:10.1016/j.combustflame.2005.02.002.

[11] P. Desgroux, A. Faccinetto, X. Mercier, T. Mouton, D. Aubagnac Karkar, and A. El Bakali. Comparative study of the soot formation process in a "nucleation" and a "sooting" low pressure premixed methane flame. *Combust. Flame*, 184:153–166, 2017. doi:10.1016/j.combustflame.2017.05.034.

[12] V. Dribinski, A. Ossadtchi, V. A. Mandelshtam, and H. Reisler. Reconstruction of Abel-transformable images: The Gaussian basis-set expansion Abel transform method. *Rev. Sci. Instrum.*, 73(7):2634–2642, 2002. doi:10.1063/1.1482156.

[13] B. Eliasson and U. Kogelschatz. Nonequilibrium volume plasma chemical processing. *IEEE Trans. Plasma Sci.*, 19(6):1063–1077, 1991. doi:10.1109/27.125031.

[14] A. Fialkov. Investigations on ions in flames. *Prog. Energy Combust. Sci.*, 23:399–528, 1997. doi:10.1016/S0360-1285(97)00016-6.

[15] S. Gibson, D. D. Hickstein, R. Yurchak, M. Ryazanov, D. Das, and G. Shih. PyAbel/PyAbel: v0.8.4, Apr. 2021.

[16] B. Giechaskiel, M. Maricq, L. Ntziachristos, C. Dardiotis, X. Wang, H. Axmann, A. Bergmann, and W. Schindler. Review of motor vehicle particulate emissions sampling and measurement: From smoke and filter mass to particle number. *J. Aerosol Sci.*, 67:48–86, 2014. doi:10.1016/j.jaerosci.2013.09.003.

[17] I. Glassman. Sooting laminar diffusion flames: Effect of dilution, additives, pressure, and microgravity. *Symp. (Int.) Combust.*, 27(1):1589–1596, 1998. doi:10.1016/S0082-0784(98)80568-7.

[18] J. Guo, J. M. Goodings, A. N. Hayhurst, and S. G. Taylor. A simple method for measuring positive ion concentrations in flames and the calibration of a nebulizer/atomizer. *Combust. Flame*, 133(3):335–343, 2003. doi:10.1016/S0010-2180(03)00020-8.

[19] M. Han, F. Yang, and H. Sun. A bibliometric and visualized analysis of research progress and frontiers on health effects caused by PM2.5. *Environ. Sci. Pollut. Res.*, 28:30595—30612, 2021. doi:10.1007/s11356-021-14086-z.

[20] A. N. Hayhurst. Mass spectrometric sampling of flames: how ionic equilibria in flames produce sampling falsifications and "fake" ions, but provide kinetic and thermodynamic data on the reaction occurring. *Prog. Energy Combust. Sci.*, 88:100927, 2022. doi:10.1016/j.pecs.2021.100927.

[21] B. Haynes, H. Jander, and H. Wagner. The effect of metal additives on the formation of soot in premixed flames. *Symp. (Int.) Combust.*, 17(1):1365–1374, 1979. doi:10.1016/S0082-0784(79)80128-9.

[22] H. Höft, M. M. Becker, and M. Kettlitz. Impact of gas flow rate on breakdown of filamentary dielectric barrier discharges. *Phys. Plasmas*, 23(3):033504, 2016. doi:10.1063/1.4943278.

[23] J. B. Howard and W. J. Kausch. Soot control by fuel additives. *Prog. Energy Combust. Sci.*, 6(3):263–276, 1980. doi:10.1016/0360-1285(80)90018-0.

[24] Y. Ju and W. Sun. Plasma assisted combustion: Dynamics and chemistry. *Prog. Energy Combust. Sci.*, 48:21–83, 2015. doi:10.1016/j.pecs.2014.12.002.

[25] R. K. A. Kailasanathan, J. Zhang, T. Fang, and W. L. Roberts. Effects of diluents on soot surface temperature and volume fraction in diluted ethylene diffusion flames at pressure. *Combust. Sci. Technol.*, 186(6):815–828, 2014. doi:10.1080/00102202.2013.878710.

[26] S. Kaiser and J. Frank. Spatial scales of extinction and dissipation in the near field of non-premixed turbulent jet flames. *Proc. Combust. Inst.*, 32(2):1639–1646, 2009. doi:10.1016/j.proci.2008.05.082.

[27] E. Karakas, M. A. Akman, and M. Laroussi. The evolution of atmospheric-pressure low-temperature plasma jets: jet current measurements. *Plasma Sources Sci. Technol.*, 21(3):10, 2012. doi:10.1088/0963-0252/24/2/025038.

[28] S. Karnani and D. Dunn-Rankin. Visualizing CH* chemiluminescence in sooting flames. *Combust. Flame*, 160(10):2275–2278, 2013. doi:10.1016/j.combustflame.2013.05.002.

[29] G. A. Kelesidis, C. A. Bruun, and S. E. Pratsinis. The impact of organic carbon on soot light absorption. *Carbon*, 172:742–749, 2021. doi:10.1016/j.carbon.2020.10.032.

[30] K. G. Kostov, M. Machida, V. Prysiazhnyi, and R. Y. Honda. Transfer of a cold atmospheric pressure plasma jet through a long flexible plastic tube. *Plasma Sources Sci. Technol.*, 24(2):025038, 2015. doi:10.1088/0963-0252/24/2/025038.

[31] K. G. Kostov, T. M. C. Nishime, M. Machida, A. C. Borges, V. Prysiazhnyi, and C. Y. Koga-Ito. Study of cold atmospheric plasma jet at the end of flexible plastic tube for microbial decontamination. *Plasma Processes Polym.*, 12(12):1383–1391, 2015. ISSN 16128869. doi:10.1002/ppap.201500125.

[32] A. Lai, M. L. Chang, R. P. O'Donnell, C. Zhou, J. A. Sumner, and T. K. Hsiai. Association of COVID-19 transmission with high levels of ambient pollutants: Initiation and impact of the inflammatory response on cardiopulmonary disease. *Sci. Total Environ.*, 779:146464, 2021. doi:10.1016/j.scitotenv.2021.146464.

[33] A. Liu, K. H. Luo, S. Rigopoulos, and W. Jones. Effects of the electric field on soot formation in combustion: A coupled charged particle PBE-CFD framework. *Combust. Flame*, page 111796, 2021. doi:10.1016/j.combustflame.2021.111796.

[34] F. Liu, Y. Hua, H. Wu, and C.-f. Lee. Effect of toluene addition on the PAH formation in laminar coflow diffusion flames of n-heptane and isooctane. *Energy Fuels*, 32(6): 7142–7152, 2018. doi:10.1021/acs.energyfuels.8b00745.

[35] Y. Liu, J. Tan, M. Wan, L. Zhang, and X. Yao. Quantitative measurement of OH^* and CH^* chemiluminescence in jet diffusion flames. *ACS Omega*, 5(26):15922–15930, 2020. doi:10.1021/acsomega.0c01093.

[36] X. Lu, M. Laroussi, and V. Puech. On atmospheric-pressure non-equilibrium plasma jets and plasma bullets. *Plasma Sources Sci. Technol.*, 21(3):034005, 2012. doi:10.1088/0963-0252/21/3/034005.

[37] M. M. Maricq. A comparison of soot size and charge distributions from ethane, ethylene, acetylene, and benzene/ethylene premixed flames. *Combust. Flame*, 144 (4):730–743, 2006. doi:10.1016/j.combustflame.2005.09.007.

[38] N. D. Marsh, I. Preciado, E. G. Eddings, A. F. Sarofim, A. B. Palotas, and J. D. Robertson. Evaluation of organometallic fuel additives for soot suppression. *Combust. Sci. Technol.*, 179(5):987–1001, 2007. doi:10.1080/00102200600862497.

[39] J. W. Martin, M. Botero, R. I. Slavchov, K. Bowal, J. Akroyd, S. Mosbach, and M. Kraft. Flexoelectricity and the formation of carbon nanoparticles in flames. *J. Phys. Chem. C*, 122(38):22210–22215, 2018. doi:10.1021/acs.jpcc.8b08264.

[40] J. W. Martin, K. L. Bowal, A. Menon, R. I. Slavchov, J. Akroyd, S. Mosbach, and M. Kraft. Polar curved polycyclic aromatic hydrocarbons in soot formation. *Proc. Combust. Inst.*, 37(1):1117–1123, 2019. doi:10.1016/j.proci.2018.05.046.

[41] J. W. Martin, M. Salamanca, and M. Kraft. Soot inception: Carbonaceous nanoparticle formation in flames. *Prog. Energy Combust. Sci.*, 88:100956, 2022. ISSN 0360-1285. doi:10.1016/j.pecs.2021.100956.

[42] I. Mulla, P. Desgroux, B. Lecordier, and A. Cessou. Comprehensive characterization of sooting butane jet flames, Part 1: Soot, soot-precursor, and reaction zone. *Combust. Flame*, 233:111595, 2021. doi:10.1016/j.combustflame.2021.111595.

[43] D. G. Park, B. C. Choi, M. S. Cha, and S. H. Chung. Soot reduction under dc electric fields in counterflow non-premixed laminar ethylene flames. *Combustion Sci. Technol.*, 186(4-5):644–656, 2014. doi:10.1080/00102202.2014.883794.

[44] A. Piel. *Plasma Physics: An Introduction to Laboratory, Space, and Fusion Plasmas*. Springer-Verlag Berlin Heidelberg, New York, NY, 1 edition, 2010.

[45] E. Place and F. J. Weinberg. Electrical control of flame carbon. *Proc. Math. Phys. Eng. Sci.*, 289(1417):192–205, 1966. doi:10.1098/rspa.1966.0006.

[46] K. Ritrievi, J. Longwell, and A. Sarofim. The effects of ferrocene addition on soot particle inception and growth in premixed ethylene flames. *Combust. Flame*, 70(1): 17–31, 1987. doi:10.1016/0010-2180(87)90156-8.

[47] M. Smooke, M. Long, B. Connelly, M. Colket, and R. Hall. Soot formation in laminar diffusion flames. *Combust. Flame*, 143(4):613–628, 2005. doi:10.1016/j.combustflame.2005.08.028.

[48] A. Starikovskiy and N. Aleksandrov. Plasma-assisted ignition and combustion. *Prog. Energy Combust. Sci.*, 39(1):61–110, 2013. doi:10.1016/j.pecs.2012.05.003.

[49] Y. Tang, J. Sun, B. Shi, S. Li, and Q. Yao. Extension of flammability and stability limits of swirling premixed flames by AC powered gliding arc discharges. *Combust. Flame*, 231:111483, 2021. doi:10.1016/j.combustflame.2021.111483.

[50] K. Walsh, M. Long, M. Tanoff, and M. Smooke. Experimental and computational study of CH, CH*, and OH* in an axisymmetric laminar diffusion flame. *Symp. (Int.) Combust.*, 27(1):615–623, 1998. doi:10.1016/S0082-0784(98)80453-0.

[51] F. J. Weinberg. Advanced combustion methods. Technical report, Imperial College of Science and Technology, London, 1986.

[52] J. Winter, R. Brandenburg, and K.-D. Weltmann. Atmospheric pressure plasma jets: an overview of devices and new directions. *Plasma Sources Sci. Technol.*, 24(6): 064001, oct 2015. doi:10.1088/0963-0252/24/6/064001.

[53] G. Xu, Y. Geng, X. Li, X. Shi, and G. Zhang. Characteristics of a kHz helium atmospheric pressure plasma jet interacting with two kinds of targets. *Plasma Sci. Technol.*, 23(9):095401, 2021. doi:10.1088/2058-6272/ac071a.

[54] Z. Zheng, W. Nie, S. Zhou, Y. Tian, Y. Zhu, T. Shi, and Y. Tong. Characterization of the effects of a plasma injector driven by ac dielectric barrier discharge on ethylene-air diffusion flame structure. *Open Phys.*, 18(1):58–73, 2020. doi:10.1515/phys-2020-0008.